Mapping Domain Structures Near a Grain Boundary in a Lead Zirconate Titanate Ferroelectric Film using X-ray Nano-diffraction

Stanislav Udovenko[1], Yeongwoo Son[1], Pannawit Tipsawat[1], Reilly Knox[1], Stephan Hruszkewycz[2], Hanfei Yan[3], Xiaojing Huang[3], Ajith Pattammattel[3], Marc Zajac[2], Wonsuk Cha[4], Darren C. Pagan[1], and Susan Trolier-McKinstry[1]

[1]Department of Materials Science and Engineering and Materials Research Institute, The Pennsylvania State University
[2]Materials Science Division, Argonne National Laboratory
[3]National Synchrotron Light Source II, Brookhaven National Laboratory
[4]X-Ray Science Division, Argonne National Laboratory

The effect of electric field on local domain structure near a 24° tilt grain boundary in a 200 nm thick $Pb(Zr_{0.2}Ti_{0.8})O_3$ (PZT20/80) bi-crystal ferroelectric film is probed using synchrotron nano-diffraction. The bi-crystal film was grown epitaxially on $SrRuO_3$-coated (001) $SrTiO_3$ 24° tilt bi-crystal substrates. From the nano-diffraction data, real space maps of the ferroelectric domain structure around the grain boundary prior to and during application of 200 kV/cm electric field are reconstructed. In the vicinity of the tilt grain boundary, the distributions of densities of *c*-type tetragonal domains with c-axis aligned with the film normal were calculated based on diffracted intensity ratios of *c*- and *a*-type domains and reference powder diffraction data. Diffracted intensity was averaged along the grain boundary, and it was shown that the density of *c*-type tetragonal domains dropped to ~50% that of the bulk of the film over a range ±150 nm from the grain boundary. This work complements previous results acquired by Band Excitation Piezoresponse Force Microscopy (BE-PFM), suggesting that reduced nonlinear piezoelectric response around grain boundaries may to be related to the change in domain structure, as well as to the possibility of increased pinning of domain wall motion. Implications of the results and analysis in terms of understanding the role of grain boundaries in affecting the nonlinear piezoelectric and dielectric responses of ferroelectric materials are discussed.

1. INTRODUCTION

Ferroelectric materials are extensively utilized in devices such as electro-mechanical actuators, transducers, sensors, and multilayer capacitors. In many ferroelectrics, domain wall motion is an important contributor to the properties; this is typically referred to as the extrinsic contribution to the properties. In particular, domain wall motion entails the redistribution of polarization and strain, and so affects the dielectric and piezoelectric responses of the material (1), (2), (3). For example, Fancher et al. reported that polarization reconfiguration due to 180° domain wall motion contributes >80% of the measured macroscopic polarization changes during switching in lead zirconate titanate (PZT) ceramics. Likewise, comparisons of X-ray diffraction and electrical polarization measurements in $BaTiO_3$ ceramics showed that ~70% of the large macroscopic dielectric permittivity in $BaTiO_3$ (0.05 kV/mm to 0.7 kV/mm) arises from domain reversal (4). Jones et al. demonstrated that ~34% of the measured piezoelectric d_{33} coefficient arose from motion of non-180° domain walls in PZT ceramics using *in situ* stroboscopic neutron diffraction data (5). Numerous other experimental and theoretical works have confirmed the important role that domain wall motion plays in macroscopic dielectric and piezoelectric response.

In bulk ferroelectrics, various crystalline defects such as dislocations, triple points, and grain boundaries may act as either pinning centers or nucleation centers for domain walls (6), (7), (8), (9). The role of grain boundaries is particularly complex. When grain boundaries act as pinning centers (10) for domain walls, they lead to reduced electromechanical and dielectric responses (11), (12), (13), (14), (15), (16). Conversely, new domains can nucleate at triple points and grain boundaries, inducing enhanced properties. However, there is little direct quantitative characterization of the domain structure changes near a grain boundary and the mobility of domain walls. A more quantitative and statistically significant understanding of the way in which individual grain boundaries with varying properties (e.g., misorientation angles or the presence/absence of a coincident site lattice) influence the extrinsic contributions to the piezoelectric response is required for optimization of ferroelectric materials.

Given the numerous reports on collective domain wall motion in perovskite ferroelectrics, it is anticipated that the *domain structure*, not simply individual domain walls, will affect the pinning at grain boundaries. For example, the domain structures often are arranged to maintain strain and polarization compatibility across the grain boundary. This, in turn, means that 90° domain walls will not form near certain types of grain boundaries (17). *These distributed domain structures are predicted to respond collectively to applied fields.* Indeed, phase-field modeling revealed a correlation between polarization switching in adjacent domains and coupling of the domain structure along grain boundaries (18), (19). Experimentally, domain walls are widely known to have some level of continuity across grain boundaries based on microscopy techniques (20), (21), (22) in both poled and unpoled ceramics, implying that the domain structures must move in some ways collectively.

Collective motion of domain walls was observed by Switching Spectroscopy Piezoresponse Force Microscopy (SS-PFM) in polycrystalline $Pb(Zr_{0.52}Ti_{0.48})O_3$ films. Domain walls were found to undergo irreversible motion in clusters that ranged from ~0.5 to 1 μm in size. This length scale considerably exceeded that of individual domain (10-30 nm) or grain sizes (~50-150 nm). This observation was attributed to correlated polarization switching (23). Band Excitation Piezoresponse Force Microscopy (BE-PFM) at lower fields can also be used to assess the irreversible to reversible Rayleigh ratio (24) for the piezoelectric response under sub-switching conditions. Regions with high ratios correspond to areas where irreversible domain wall motion is favorable. It was shown that the cluster size for correlated motion of domain walls in PZT films was independent of whether the film was donor or acceptor doped (25). BE-PFM results have also shown spatial clustering of non-linearity in the piezoelectric coefficients of clamped polycrystalline and epitaxial ferroelectric films (26). Observation of clusters with increased nonlinear response with sizes significantly larger than the grain size suggests that the collective domain wall motion in different grains within a cluster contributes to Rayleigh behavior in PZT films (27).

Electron microscopy has been utilized for direct observation of domain wall motion in ferroelectric capacitors. For example, in {100} oriented 100 nm thick $Pb(Zr_{0.2}Ti_{0.8})O_2$ epitaxial films grown on (001) Nb-doped $SrTiO_3$ substrates, *a*-domains in the pristine sample were split into smaller *a*- and *c*-domains on poling, forming 90˚ strip domain structures. *c*-domains are those with the polarization parallel to the substrate normal; domains with their *c*-axis aligned within the sample plane are *a*-domains. It was confirmed that 180˚ polarization switching contributed significantly to the out-of-plane polarization switching (28). Ferroelectric domain patterns in

$Pb(Zr_{0.8}Ti_{0.2})O_3$ and $Pb(Zr_{0.65}Ti_{0.35})O_3$ (PZT65/35) were analyzed using Transmission Electron Microscopy (TEM) (29). Electric fields at $Pb(Zr_{0.2}Ti_{0.8})O_3$ film/electrode interfaces have been observed by *in situ* TEM and are expected to affect the nucleation and growth rate of ferroelectric domains as well as the orientation and mobility of domain walls (7). Though there are many other reports that use TEM to explore domain switching and nucleation and motion of domain walls (30), the statistical sampling of electron microscopy techniques tends to be small since only small volumes of material can be analyzed.

Piezoresponse Force Microscopy (PFM) has also been used to study extrinsic contributions to piezoelectric properties at individual grain boundaries and triple points; this approach can sample a larger number of domain walls interacting with a given grain boundary (31) (32) (33) (34). These studies established that the extrinsic contributions to the piezoelectric response vary in the range of tens of nm to nearly a micron away from microstructural features, depending on the grain boundary character. However, with PFM it is not possible to sample the domain structure through the volume of the film. As a result, changes in domain structure (and hence domain wall density) and in domain wall mobility (via pinning) could not be deconvolved in assessing the extrinsic contributions to piezoelectric and dielectric responses of ferroelectric material locally.

Additionally, synchrotron X-ray mapping techniques have been used to probe the domain structure of ferroelectric materials. Dark Field X-ray Microscopy (DFXM) allows the distribution of strain in crystalline samples to be characterized (35). Simons et al. demonstrated the feasibility of using DFXM to examine strain fields around domain walls in $BaTiO_3$ (36). However, current limitations on X-ray optics preclude distinguishing nanoscale domains in ferroelectrics. Furthermore, DFXM is generally limited to fixed fields of view of tens of microns, again dictated by optics. Beyond DFXM, Vakhrushev et al. utilized angular splitting and the intensity of Bragg reflections to determine the population of ferroelectric domains in the rhombohedral phase of $Pb(Zr_{0.976}Ti_{0.024})O_3$ (PZT2.4) single crystals. Based on the distribution of diffuse scattering, the positions of antiphase domain boundaries were identified (37), (38). Nano-diffraction based techniques such as Scanning Transmission X-ray Microscopy (STXM) and Nano X-ray Diffraction are utilized for examination of fine structure features of nanocrystals and nanoscale devices (39) (40). *In situ* variation of sample environments (such as temperature, electric field) provides additional insight into the origin of material properties (39), (41), (42).

This paper explores the evolution of nanoscale domain structure in PZT piezoelectric bi-crystal thin films using synchrotron nano-diffraction. A custom sample assembly design is presented along with examination of PZT bi-crystal domain structure evolution under applied electric field. The *in situ* nano-diffraction results were found to be heavily influenced by the domain structure of the as-deposited condition.

2. SAMPLE PREPARATION AND CHARACTERIZATION

A custom sample assembly was designed for *in situ* application of an electric field to bi-crystal PZT specimens during nano-diffraction experiments. Figure 1 shows a labeled, exploded view of the complete sample assembly.

The PZT bi-crystal studied in this work was grown on (001) $SrTiO_3$ (STO) 10×10×0.5 mm bi-crystal substrates (MTI Corp.) with an in-plane tilt misorientation angle of 24°. Epitaxial films were deposited on the bi-crystal substrate via pulsed laser deposition with a KrF excimer 248 nm laser (Lambda Physik Complex Pro). First, a 50 nm $SrRuO_3$ (SRO) bottom electrode was deposited from a ceramic target (Kojundo Chemical Lab. Co., Ltd.) using a laser energy density of 1.5 J/cm^2, a laser pulse frequency of 4 Hz, a substrate temperature of 665°C, a target-substrate distance of 6.7 mm, and a chamber oxygen pressure of 120 mTorr. The deposition of the bottom electrode was followed by deposition of a $Pb(Zr_{0.2}Ti_{0.8})O_3$ (PZT20/80) film also from a ceramic target. To prepare the target, raw materials (Pb_3O_4, ZrO_2, TiO_2) in Pb:Zr:Ti mol% ratios of 60:10:40 were ball-milled and the resulting powder was calcined at 900°C for 4 hours. The target was formed from the ball-milled powder using a cold isostatic press for 1 minute at a pressure of 30 MPa, then sintered at 1050°C for 2 hours. Deposition of a 200 nm PZT20/80 film was performed at a laser energy density of 1.5 J/cm^2, a laser pulse frequency of 10 Hz, a substrate temperature of 600°C, a target-to-substrate distance of 6.2 mm, and a chamber oxygen pressure of 85 mTorr. This process produced a sample in which the grain boundary propagated from the substrate through both epitaxial films.

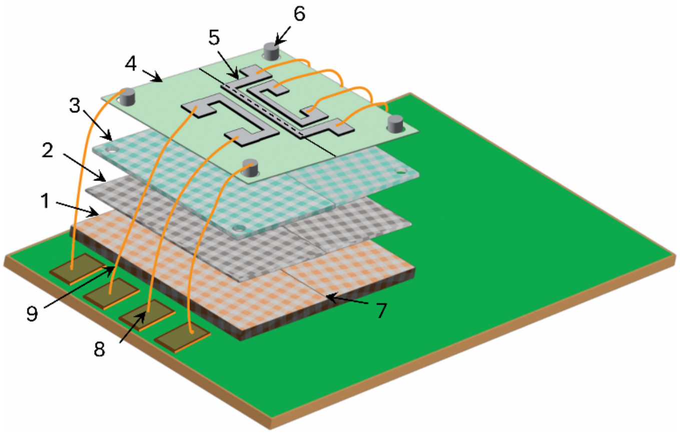

1. Strontium titanate substrate 10x10x0.5 mm
2. Strontium ruthenate bottom electrode 50 nm
3. PZT 20/80 film 200 nm
4. SiO_2 insulation layer 100 nm
5. Pt/Ti top electrodes and contact pads 50/5 nm
6. Pt/Ti bottom electrodes 50/5 nm
7. Grain boundary
8. Gold plated PCB contact pads
9. Gold wires 20 µm

Figure 1. Labeled, exploded view of the sample assembly.

To minimize the possibility of an electrical short to the bottom electrode for the large contact pads, an SiO_2 layer was patterned over the top surface of the sample using the lift-off method. For the lift-off re-entry profile, LOR 5A photoresist was initially spun at 4500 rpm for 45 seconds and baked at 180°C for 3 minutes. This was followed by spinning SPR3012 photoresist at 4500 rpm for 45 seconds and baking it at 95°C for 1 minute. The resist stack was exposed at 220 mJ/cm^2 and developed in CD26 for 80 seconds. The sample was then ashed. Subsequently, a 100 nm thick SiO_2 insulator layer was deposited by an electron beam evaporator (Kurt J. Lesker Lab-18) at a rate of 2 Å/s at room temperature. The sample was then soaked in a PRS-3000 bath at 80°C to lift off the SiO_2.

To expose the $SrRuO_3$ bottom electrode for electrical contact, a 2.5 µm thick photoresist (SPR955) was spun on the sample at 2500 rpm, then baked for 1 minute at 105°C. Subsequently, the photoresist was exposed with the desired pattern using a Heidelberg Instruments MLA-150 direct write tool at 400 mJ/cm^2; the resist was developed in CD26 for 90 seconds. Before etching, the sample was cleaned with oxygen plasma for 2 minutes with 200 sccm of O_2 and 50 sccm of He at 550 mTorr and 200 W RF power. The PZT thin film was then patterned using an ULVAC NE-550 Inductively Coupled Plasma – Reactive Ion Etch (RIE-ICP) tool. Etching was done using a chamber pressure of 3.8 mTorr with 10 sccm of Ar, 7 sccm of CF_4, and 3.5 sccm of Cl_2 at 600 W RF power, a bias power of 150 W, and an etching time of 150 seconds. Following this, the photoresist was stripped by immersing the sample in a PRS-3000 bath at 80°C.

Patterning of the strip-shaped top electrodes was done using the MLA-150 direct write tool after alignment to the grain boundary was done via an optical microscope. Finally, the top and bottom electrode layers were deposited using a DC magnetron sputter tool (Kurt J. Lesker CMS-18) and patterned using the lift-off method. The top electrode consisted of 5 nm Ti and 50 nm of Pt; the depositions were carried out at room temperature without breaking vacuum. Active electrodes measuring 2700×5 μm were prepared along the center of the PZT grain boundary. 500×500 μm square contact pads and contact traces connecting the strip electrodes to the contact pads ran on top of the SiO_2 layer. The samples were then affixed to custom printed circuit boards (PCBs) using silver paste.

After the electrodes were deposited, electrical characterization of the sample was performed on an additional round electrode placed away from the grain boundary. Figure 2 shows the polarization versus electric field hysteresis loop of the sample measured at 10 kHz at a temperature of 20˚C. As the hysteresis loop shows, the positive and negative coercive fields E_c^+ and E_c^- were 90 kV/cm and -142 kV/cm, respectively and the remanent polarization was 70 μC/cm^2. The negative bias indicates an internal field E_i of -19 kV/cm calculated using Equation (1) following (43).

$$E_i = \frac{+E_c - |-E_c|}{2} \tag{1}$$

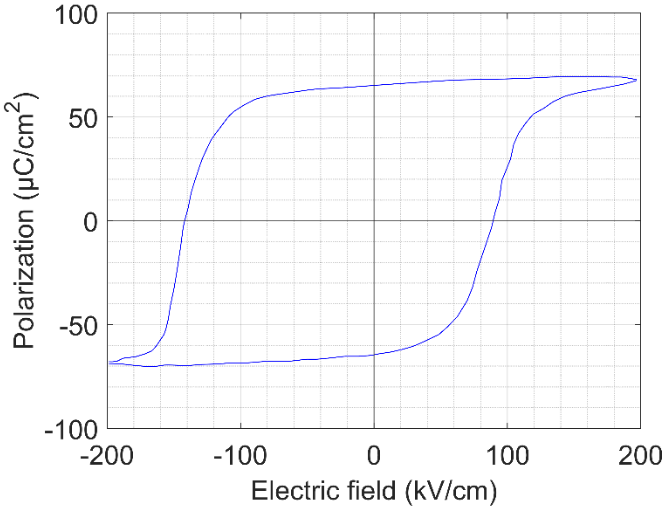

Figure 2. PZT20/80 film polarization - electric field hysteresis loop measured at 20°C and 10 kHz.

The measured sample capacitance indicated a dielectric constant of ~136 and a loss tangent of 0.05. According to reference (44), internal electric fields, such as that observed in the film tested, stabilize the domain structure against weak applied DC fields. However, in the synchrotron experiment, large DC fields were applied to the sample, so this domain structure stabilization effect should be negligible.

Laboratory source X-ray diffraction (X'Pert^3 MRD diffractometer with Cu Kα radiation) performed in a reflection geometry confirmed that the PZT films were phase-pure perovskite and had tetragonal symmetry (*P4mm* space group) as expected based on the Zr/Ti ratio. Figure 3 shows the intensity versus 2θ angle in a region containing STO, SRO, and PZT20/80 peaks. Note that the PZT 200 and SRO 200 peaks overlap. The films are structurally relaxed as seen from the relatively broad diffraction peaks, which is expected due to the significant lattice mismatch between the three materials at room temperature. In Figure 3, the 002 PZT peak has significantly higher intensity than the 200 peaks, indicating the film is predominantly composed of domains with their c-axis aligned with the sample surface normal. This higher volume fraction of c-domains is consistent with the PZT film being under finite compressive stress since the thermal expansion coefficient of the $SrTiO_3$ is higher than that of the PZT20/80. As described elsewhere (45), (46), (47), films of this composition cooled through the ferroelectric transition temperature under compressive stress tend to be predominantly composed of out-of-plane-oriented c-domains.

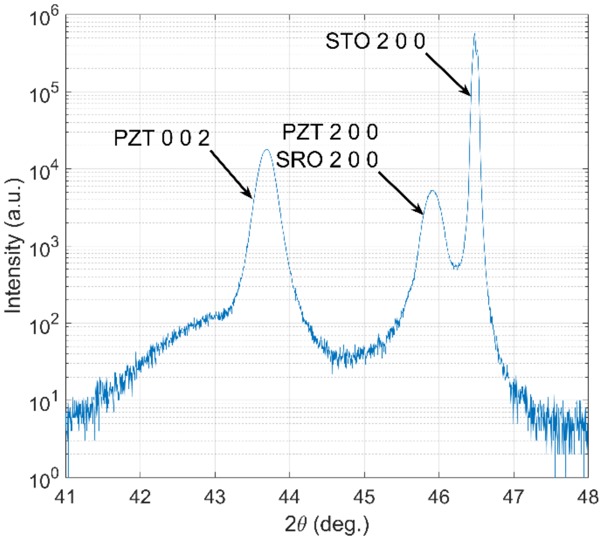

Figure 3. One-dimensional diffraction pattern of intensity versus 2θ from the PZT/SRO/STO film stack on a logarithmic scale.

Crystallinity (or mosaicity) of the film and substrate were determined by rocking the sample across the angle Ω to measure the distribution of intensity perpendicular to the radial direction of reciprocal space. Figure 4a presents a rocking curve related to the 200 STO substrate peak, while Figure 4b shows a rocking curve for the 002 PZT peak. In both figures, the Full-Width-at-Half-Maximum (FWHM) of the peaks are labeled. The FWHM of the PZT 002 peak confirms reasonable crystallinity of the deposited PZT film.

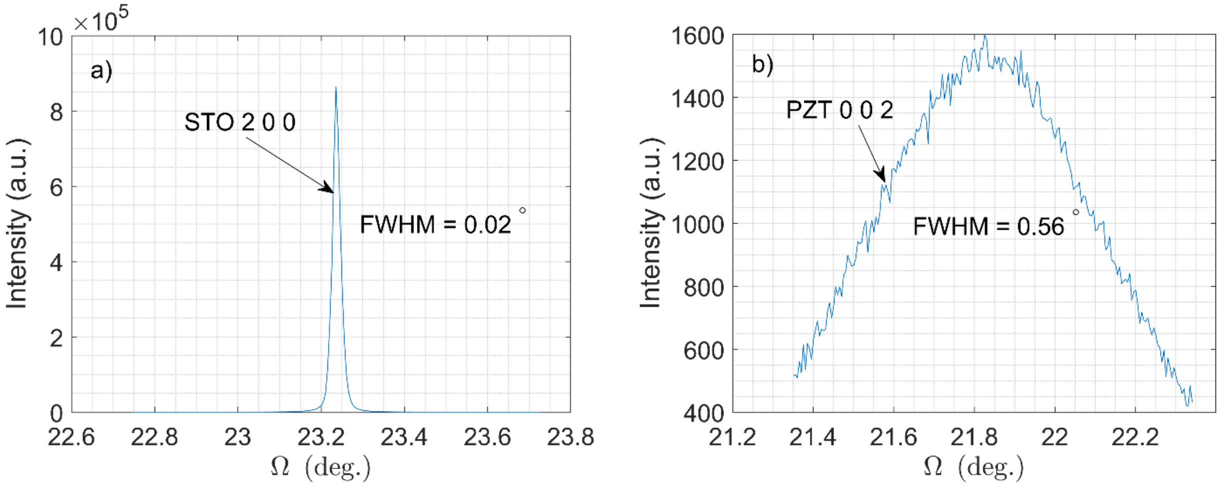

Figure 4. Rocking curve of 200 diffraction peak of STO substrate (a), rocking curve of 002 diffraction peak of PZT film (b).

3. SYNCHROTRON NANO-DIFFRACTION MEASURMENTS

The synchrotron experiment was performed at the 3-ID Hard X-ray Nanoprobe (HXN) beamline at the Brookhaven National Laboratory Synchrotron Light Source II (NSLS-II). A schematic layout of the experimental and sample geometry is provided in Figure 5 with the laboratory ($\boldsymbol{xyz}$) and sample ($\boldsymbol{x'y'z'}$) coordinate systems labeled. The incoming X-ray beam travels along the $\boldsymbol{z}$ - axis. The angle 2θ (twice the Bragg angle) is the angle between the incoming and diffracted beams. Measurements were performed in a horizontal scattering geometry with the PZT film normal placed in the horizontal scattering plane. The relationship between the scattering angle and lattice plane spacing is given by Bragg's law:

$$\lambda = 2dsin(\theta) \qquad (2)$$

where λ is the wavelength of the incoming X-ray beam and d is the lattice plane spacing.

The sample was placed in an He-filled chamber along with the focusing X-ray optics. Focusing was achieved by a Fresnel Zone Plate with a 30 nm outmost zone width, which focused the incoming beam to about 37×37 nm with a numerical aperture of 1.8×10^{-3} radians. The incoming X-ray beam energy was 11.6 keV (λ =1.069 Å). The working distance between the specimen and the order sorting aperture was approximately 10 mm. The specimen sat on a positioning stack consisting of a hexapod for coarse specimen alignment and sample rotation that supported a set of piezoelectric motors for fine specimen translations and sample scanning. The sample was rotated by angle θ about the $\boldsymbol{y}$ - axis.

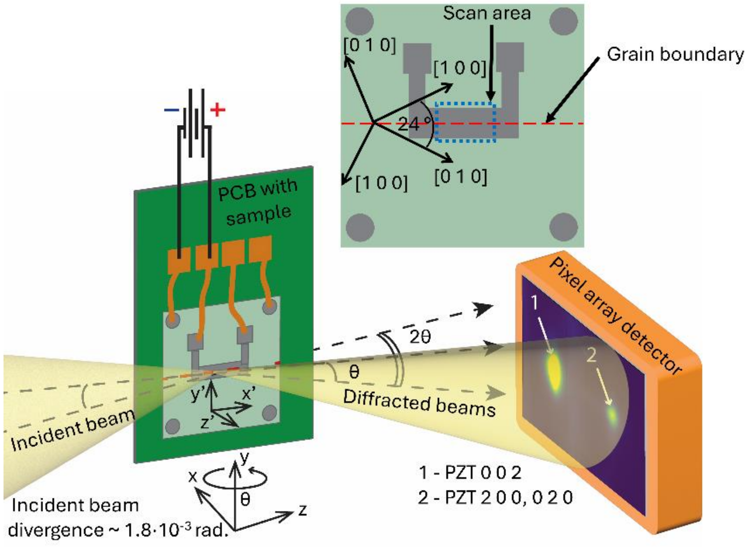

Figure 5. Experimental setup for the nano-diffraction measurements. The laboratory coordinate system is labeled $\boldsymbol{xyz}$*; the sample coordinate system is labeled* $\boldsymbol{x'y'z'}$*. Diffracted intensity is emitted at an angle* 2θ *from the incoming X-ray beam. The 002 PZT (1) and 200 PZT (2) diffraction peaks on the pixel array detector are labeled.*

Three different detectors were utilized during the experiment: a two-dimensional pixel array detector for diffraction measurements (Merlin4X, 512×512 pixels, 55 μm pixel size), an energy-dispersive silicon drift detector for fluorescence (Vortex ME3), and an imaging detector comprised of a coupled scintillator and optical camera (Prosilica) to roughly position the sample assembly with respect to the beam. The imaging detector was used to locate a corner of the sample substrate. From there, the sample was translated such that the beam was approximately in the center of the bi-crystal PZT film. The top electrode was then located by performing a 2D grid scan over the specimen surface while collecting fluorescence data. The electrode position was precisely determined by the Pt fluorescence signal. It is noted that the large sample size relative to the typical sample size for this X-ray microscope precluded the ability to place the diffraction volume directly over the rotation axis, so the sample unavoidably precessed and shifted during rotation about the $\boldsymbol{y}$ – axis.

Once the beam was aligned to the electrode (and the underlying grain boundary), the diffraction detector was positioned to subtend the PZT 200 and 002 diffraction peaks. First, the sample was rotated to $\theta = 15°$ to place the STO 002 lattice planes into the diffraction condition. The detector was then shifted to a sample to detector distance of 500 mm (sufficient to separate the 200 and 002 PZT diffraction peaks) and then moved horizontally until the intensity from the STO 200 peak was measured. The detector was then shifted until the $SrTiO_3$ 200, PZT 200, and PZT 002 peaks could all be simultaneously captured on the detector panel.

Of note is the footprint of the incoming X-ray beam on the specimen, as this plays a major role in defining the diffraction volume size, spatial resolution, and illumination of domains, along with the interpretation of diffracted intensity magnitudes. Given the angle of incidence, the beam footprint had an oval shape with a major axis determined by:

$$x = x_0/sin(\alpha) \quad (3)$$

where x is the footprint, x_0 describes the normal-incidence beam size, and α is the angle of incidence (in this case equivalent to the angle θ). For these measurements, α ~15°, which extends the beam by a factor of 4 along **x'**, producing a beam footprint of 143×37 nm along $\boldsymbol{x'}$ and $\boldsymbol{y'}$. Figure 6 illustrates the transformation of the beam footprint according to Equation 3 and the resulting diffraction volume. Due to the film thickness, domain wall inclination, angle of incidence, and finite beam size, multiple domain types can be illuminated despite the nano-focused X-ray probe.

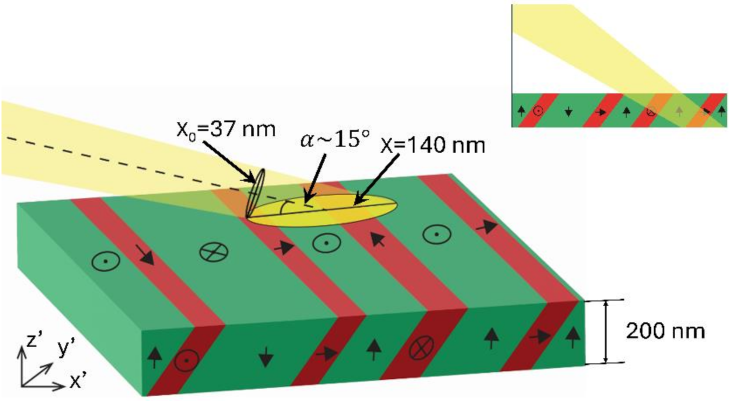

Figure 6. Schematic illustration of the incident beam footprint transformation according to Equation 3 and its effect on the illuminated diffraction volume. Green corresponds to c-domains and red corresponds to a-domains. Inset shows the path of the X-ray beam through the film.

The system for *in situ* application of the electric field included a Keysight Keithley 4980A precision LCR meter, a Raspberry Pi 4B single-board computer, a 16-channel relay module (Sainsmart), and a power supply (Alitove). The system was controlled via the Raspberry Pi 4B and a custom Python script. The LCR meter served as a voltage source and enabled continuous measurement of voltage, capacitance, and dielectric loss during application of an electric field. Electric fields were applied between the top and bottom electrodes along the **z'** axis corresponding to the film normal direction (see Figure 5). The LCR meter was connected to the sample through a relay module placed inside the sample chamber. The relay module controlled which electrode on the sample was active. Figure 7a shows the setpoint and measured values of the electric field E as a function of time through the experiment. In Figure 7a, one can see that, upon increasing the electric field, the difference between the set value of the electric field and measured electric field increased due to an increase in the sample leakage current. Similarly, Figure 7b shows the sample's capacitance and dielectric losses. The capacitance peaked directly after switching of the electric fields. Dielectric losses grew on increasing electric field, while the region of high amplitude and frequency of oscillations of the dielectric loss observed at maximum electric field (200 kV/cm) may indicate that the sample was close to electrical breakdown.

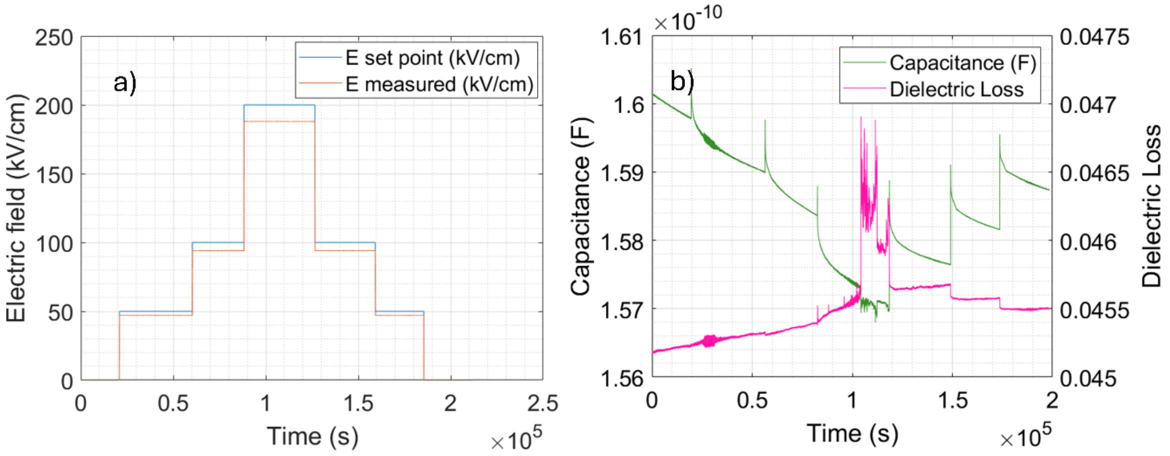

Figure 7. Electric field set point (blue line), measured electric field in sample (orange line) (a); sample's capacitance (green line), dielectric losses of sample (purple line) (b). The AC excitation signal used for the permittivity measurements was 50 mV and a frequency 2 MHz.

Diffraction scans were performed on the specimen at each increment of electric field (0, 50, 100, 200, 100, 50, 0 kV/cm). However, the analysis here focuses on application of the peak field where the evolution of the domain structure was expected to be largest. A diffraction scan consisted of rotating the specimen across a sequence of θ angles between the range of 14.5° and 16° in 0.25° increments. At each θ angle, diffraction patterns were measured on a grid of points in the **x'-y'** plane. The grid spanned 6×5.1 μm with measurement spacing of 30 nm for a total of 200×170 (34,000) diffraction patterns. Critically, the experimental configuration and sample design precluded registration of the specimen along the electrode / grain boundary as extra fiducials were not deposited. For this reason, shifts of the sample along $\boldsymbol{x'}$ during application of electric field or due to sample rocking could not be corrected, leading to motion of the scan region of the sample.

To reduce measurement diffraction detector data size, only a 509×289 pixel sub-region that contained the $SrTiO_3$ 200, PZT 200, and PZT 002 peaks were saved. Peak intensity of the 200 PZT peak (corresponding to *a*-domains) was measured at $\theta = 15.85^\circ$ and peak intensity of the 002 PZT peak (corresponding to *c*-domains) was measured at $\theta = 14.80^\circ$. Processing of the diffraction data was performed using a set of Python scripts described in more detail in the next section. Prior to processing, diffraction patterns were normalized by the incoming beam flux.

4. ANALYSIS AND RESULTS

a) Spatial Distributions of Scattering Features

To gain insight into the real space domain structure, the series of diffraction patterns were processed to build spatial maps of various reciprocal space intensity features. The diffraction images used to generate these maps at $\theta = 15.85^\circ$ and at $\theta = 14.80^\circ$ corresponded to the peak intensity of the 200 and 002 PZT diffraction peaks which in turn were associated with scattering from a-domains and c-domains. The primary scattering at the center of the diffraction peak associated with the bulk of the illuminated domains was separated from diffuse scattering associated with distorted regions of the domains (i.e., regions near domain walls). Extraction of intensity of interest from the diffraction patterns was performed using binary masks. Primary scattering (marked with red dashed boxes) and diffuse scattering (marked with green dashed-boxes) mask regions are shown on representative images for scattered intensity from a-domains and c-domains in Figures 8a and 8e, respectively. In these diffraction images, the horizontal direction corresponds to the radial direction in reciprocal space associated with variation in lattice plane spacing, while the vertical direction corresponds to variation in lattice plane normal orientation.

The diffracted intensity within the masks was summed on each diffraction image and then mapped to the grid of measurement points in real space (200×170 points with 30 nm spacing). Figures 8b and 8f show the summed intensity from the primary scattering masks around the PZT 200 and 002 peaks at $\theta = 15.85°$ and $\theta = 14.80°$, respectively. In these figures (and Figures 8c, 8d, 8g, and 8h), the maximum intensity of the color scale varies in order to improve feature contrast. Also note that these two real space maps correspond to different regions along the electrode (due to specimen shifts during rocking). In Figure 8b, one can see a stripe structure that forms at angles close to 24˚, which corresponds to the angle of in-plane misorientation of the bi-crystal sample film. Within each spatial map (140×37×200 nm), there is non-zero intensity at all points, indicating both a- and c-domains are generally present. However, for most points on the spatial maps, c-domains are dominant. In Figure 8f, one can note the existence of "islands" of regions of elevated intensity that correspond to significantly increased presence of c-domains and reduced presence of a-domains.

Figures 8c and 8g show the summed intensity from the same two scans in Figures 8b and 8f, but instead using the diffuse masks (marked with green dashed boxes). Taking into account the orientations of domain walls in bi-crystal PZT films with the same composition measured by PFM (32), (33), (34), one can suggest the diffuse scattering is associated with distorted crystal near domain walls. Increased diffuse scattering can also be observed near the grain boundary in Figure 8c, which is consistent with the primary contributor to the diffuse scattering being distorted regions of crystal. Figures 8d and 8h show the distribution of primary peak intensity divided by the distribution of intensity scattered by domain walls, providing a merged view of the domain composition and wall structure. By dividing primary scattering, mainly from the bulk of domains, by the diffuse scattering, mainly from the domain walls, further feature enhancement is achieved to observe the domain structure present.

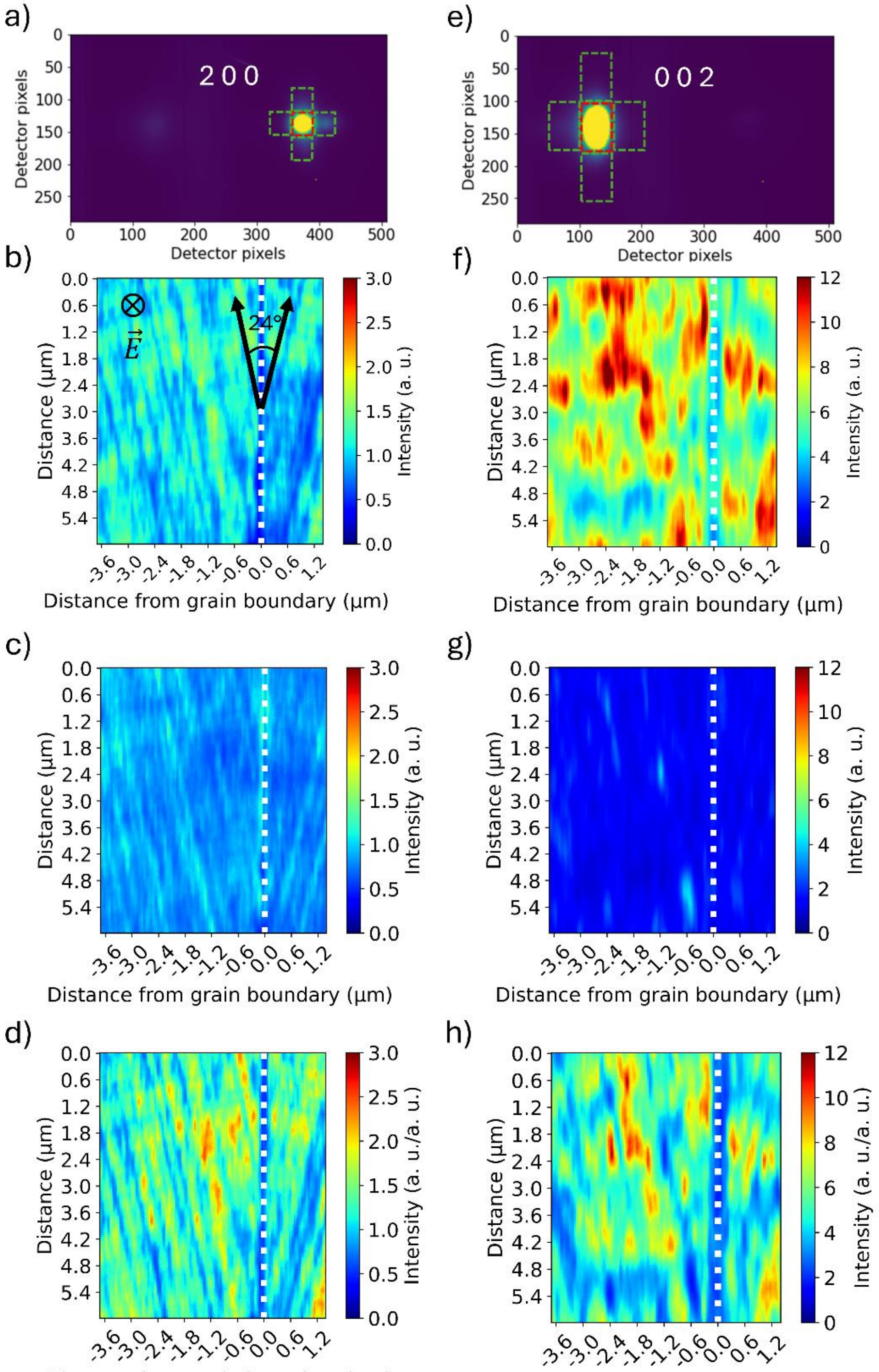

Figure 8. Representative diffraction patterns measured at 0 kV/cm, including a-domain peak (a) and c-domain peak (e) with masks; distribution of primary peak intensity for a- and c- domains ((b), (f)); distribution of diffuse scattering from microstructure features around a-domain peak and c-domain peak ((c), (g)); distribution of primary intensities divided by diffuse scattering ((d), (h)) Grain boundary position shown with white dotted lines and Figure 8b indicates the 24° angle between [100] directions on the STO bi-crystal on which the epitaxial PZT was grown..

b) Domain Structure Characterization Under Applied Field

The average response of all scanned regions as the sample was rocked in 2θ was evaluated to probe bulk domain switching and facilitate segmentation between regions primarily comprised of *a*- or *c*-domains. First, 1D intensity line profiles were constructed by summing the 2D diffraction images perpendicular to the radial direction in reciprocal space to collapse the data onto the 2θ axis, then summing across all scan points and θ angles. Figure 9 shows the summed intensity of the STO, SRO and PZT Bragg peaks versus lattice plane spacing (2θ transformed to d using Equation 2) for both 0 and 200 kV/cm applied to the PZT bi-crystal film. As can be seen, there is a broadening of the PZT 200 and 002 diffraction peaks with applied field. This is believed to be from an increase in strain heterogeneity arising from the need to maintain deformation compatibility (48).

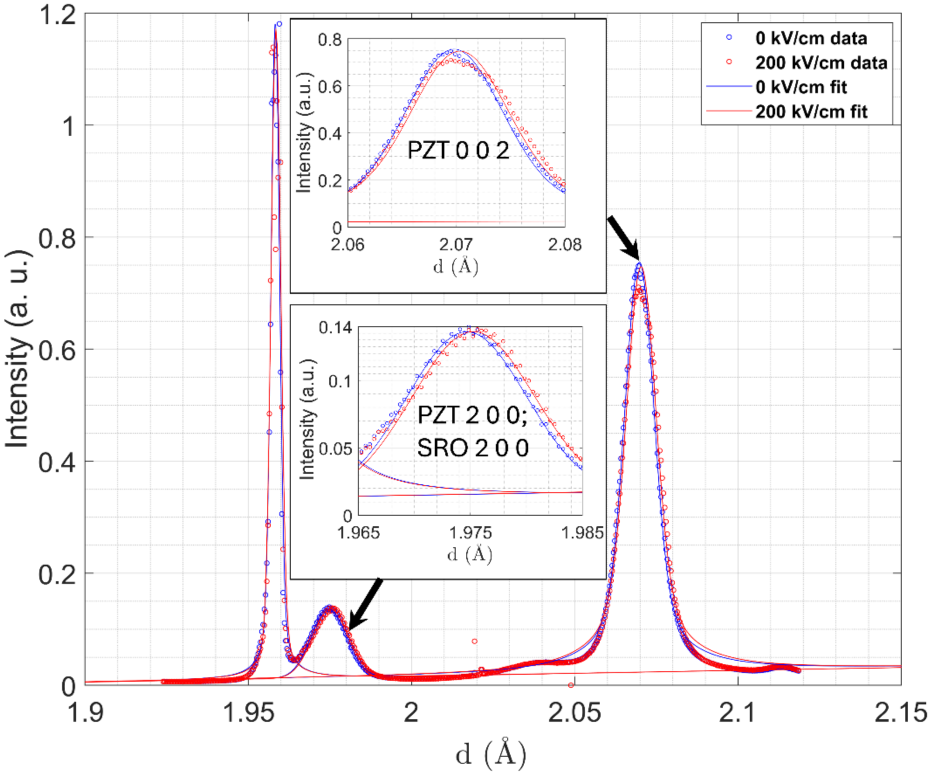

Figure 9. *Integrated 1D diffraction patterns (circles) and corresponding peak fits (solid lines) from the PZT bi-crystal film collected at 0 and 200 kV/cm (blue and red colors respectively).*

The 002 and 200 diffraction peaks were fit with pseudo-Voigt functions to establish the mean position associated with the average lattice plane spacing $\bar{d}$ and the total integrated intensity I. Analysis of the PZT 002 (*c*-domain) peak position showed the peak shift to higher lattice plane spacing values at an electric field of 200 kV/cm compared to zero field. The intrinsic piezoelectric strain ε was calculated from the peak positions using the relationship:

$$\varepsilon = \frac{\bar{d} - \bar{d}_0}{\bar{d}_0} \tag{4}$$

where $\bar{d}$ is the mean lattice plane spacing under applied field and $\bar{d}_0$ is the mean lattice plane spacing prior to application of field. The intrinsic piezoelectric strain was calculated to be 2.6×10^{-4} with the uncertainty of the strain determined from fit peak position estimated to be 2×10^{-6} following (49). Using this strain, the value of $d_{33,f}$ was evaluated as:

$$d_{33,f} = \frac{\varepsilon}{\Delta E} \tag{5}$$

where ΔE is the increase in applied electric field. This analysis gives $d_{33,f}$ as 13 ± 0.1 pm/V, which is commensurate with the value of 10 pm/V found in the literature (50). A concurrent shift in the peak corresponding to *a*-domains was attributed to the "passive" elongation of *a*-domains caused by the need to maintain deformation compatibility with adjacent *c*-domains. This model is consistent with prior reports by Pramanick et al. (51).

The volume fraction of *c*-domains, υ_{002}, was calculated from the 1D line profiles in Figure 9 using the formula (details in (52), (53)):

$$\upsilon_{002} = \frac{I_{002}/I'_{002}}{I_{002}/I'_{002} + 2\, I_{200}/I'_{200}} \tag{6}$$

where I_{hkl} is the integrated intensity of the diffraction peak from the sample and I'_{hkl} is the reference value of intensity from the powder diffraction data (54). The population of *c*-domains with polarizations perpendicular to the film surface was close to 87% at both 0 kV/cm and 200 kV/cm. The relatively minimal change of the bulk volume fractions of the domains due to substrate constraints is noted; however, this does not preclude reconfiguration of the domain structure (as will be seen). Figure 10 shows real space maps corresponding to 0 kV/cm (a) and 200 kV/cm (b).

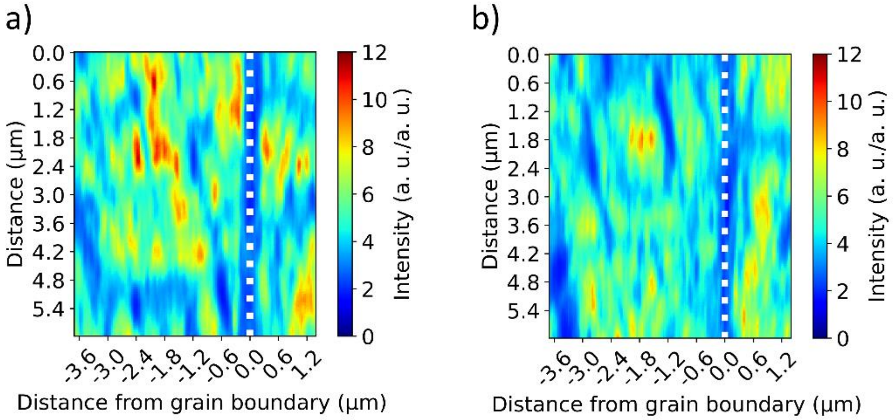

Figure 10. Primary scattering intensity maps associated with c-domains at 0 kV/cm and 200 kV/cm shown in (a) and (b), respectively. The white dotted line represents the position of the grain boundary.

To more closely analyze *c*-domains as a function of distance from the grain boundary and electric field, the intensity distributions shown in Figure 10 were summed parallel to the grain boundary (vertical dotted line). Figure 11 shows the diffracted intensity associated with *c*-domain density distribution perpendicular to the grain boundary at 0 kV/cm (blue line) and at 200 kV/cm (orange line). From Figure 11, one can clearly see that, away from the grain boundary, the density of c-domains is relatively high regardless of applied field. Also of note is a decrease in the intensity (v_{002}) within ±150 nm of the grain boundary as determined from a 50% decrease in intensity associated with c-domains. The high-density of c-domains in the sample volume (v_{002}) is consistent with the film being in a compressive stress state as described above. As was observed with the global volume fraction measurements, there is minimal change in the total intensity with an applied field. The small reduction of intensity with field, the reverse of expected behavior, is due to the previously mentioned shift of the scanned region on the sample, not a decrease in c-domain volume fraction. The observed change in the domain state must be one of the contributors to the report of Marincel et al. on reduced irreversible to reversible Rayleigh ratios at comparable bi-crystal boundaries (32), (33), (34). This suggests that, in order to fully understand the role that domain walls play in the extrinsic contributions to the piezoelectric and dielectric responses, it will be important to understand not just the local Rayleigh behavior, but also the local domain structure. Local diffraction methods provide a method to assess the latter *quantitatively*, in a way which is currently challenging to do with other techniques.

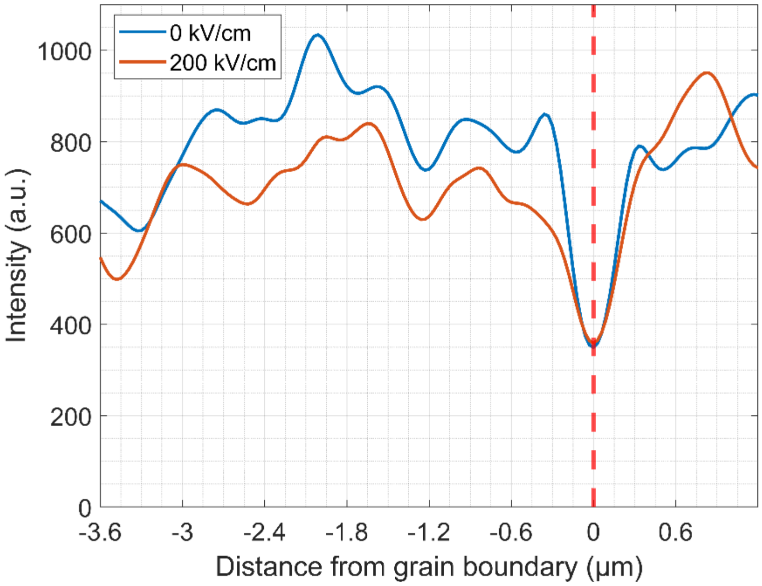

*Figure 11. Diffracted intensity related to scattering of c-domains (Figures 10a and 10b) integrated along grain boundary direction (**x'**).*

5. CONCLUSIONS

Domain structure in a 200 nm bi-crystal PZT20/80 film was probed via X-ray nano-diffraction around a 24° tilt grain boundary under controlled out-of-plane applied electric field. It was found that the separation of primary and diffuse scattering around diffraction peaks facilitated identification of domain structure features. An analysis of the domain densities as a function of distance from the grain boundary revealed a significant drop in the volume fraction of c-type tetragonal domains to ~50% within ±150 nm from the grain boundary. The total high volume fraction of *c*-domains (~87%) is due to compressive stress from the STO substrate. In addition, measurements showed that the *c*-domains in the as-deposited sample evolved little during application of 200 kV/cm due to clamping by the substrate.

The measurements shown here highlight fundamental challenges for direct characterization of domain structure using nano-diffraction that require consideration. The combination of achievable beam footprint, through-thickness penetration, and domain wall orientation (here parallel to {101} lattice planes) likely precludes isolation of single domains when probing realistic ferroelectric films (illustrated in Figure 6). In the data presented, varying intensity associated with *c*-domains was measured in every probed diffraction volume (see Figure 10), indicating that *a*- and *c*-domains were generally always illuminated. Thus, for more quantitative measures of domain composition in each diffraction volume, simultaneous mapping of real space and reciprocal space through measurements of rocking curves at each measurement point is necessary. With these measurements, local volume fractions, in addition to quantities such as local strain state, would be probed. These measurements are possible but require position stability or re-registration that was not performed here due to sample design, but which can be addressed in the future. In addition, a relatively thin (200 nm) film was selected for study to minimize the number of domains illuminated during measurement. This led to a large initial volume fraction of *c*-domains and minimal evolution of this quantity with electric field due to substrate clamping. Increasing film thickness to alleviate the clamping will provide further insights into domain wall behavior near grain boundaries, but also increase the number of domains illuminated within each diffraction volume, further supporting the need for the combined real space / reciprocal space approach for mapping domain structure as advocated above.

Of particular interest in the future will be characterizing a much wider array of grain boundary angles and types to explore the fundamental materials science associated with reconfigurations of the domain states associated with microstructural features. There is currently a dearth of direct, *in situ* structural data at grain boundaries contributing to an incomplete understanding of nature of nonlinearity suppression mechanisms in ferroelectric films. It is still an open question as to whether variation of domain wall structure or mobility contributes to reduced d_{33} values observed at grain boundaries, but here, differences in domain structure (variation of relative volume fractions of *a*- and *c*-domains) at the grain boundary were observed.

ACKNOWLEDGEMENTS

This work was supported by the US National Science Foundation: DMR-2025439. This research used the Hard X-ray Nanoprobe beamline at the National Synchrotron Light Source II, a U.S. Department of Energy (DOE) Office of Science User Facility operated for the DOE Office of Science by Brookhaven National Laboratory under Contract No. DE-SC0012704. Work by S.O.H (contributions to data analysis and manuscript preparation) was supported by U.S. Department of Energy, Office of Science, Basic Energy Sciences, Materials Science and Engineering Division. Authors also would like to thank Dmitry Chernyshov (SNBL at ESRF, France) for discussions that helped a lot in data analysis.

REFERENCES

1. **A. Tagantsev, L. Cross, J. Fousek.** *Domains in ferroic crystals and films.* New-York : New York: Springer, 2010.

2. **B. Jaffe, W. Cook, H. Jaffe.** *Piezoelectric ceramics.* New-York : London and New-York: Academic Press, 1972.

3. *Direct evaluation of domain-wall and intrinsic contributions to the dielectric and piezoelectric response and their temperature dependence on lead zirconate-titanate ceramics.* **Q. Zhang, H. Wang, N. Kim, L. Cross.** 1, 1994, J. Appl. Phys., Vol. 75, pp. 454-459.

4. *The contribution of 180° domain wall motion to dielectric properties quantified from in situ X-ray diffraction.* **C. Fancher, S. Brewer, C. Chung, S. Röhrig, T. Rojac, G. Esteves, M. Deluca, N. Bassiri-Gharb, J. Jones.** 2017, Acta Mater., Vol. 126, pp. 36-43.

5. *Direct measurement of the domain switching contribution to the dynamic piezoelectric response in ferroelectric ceramics.* **J. Jones, M. Hoffman, J. Daniels, A. Studer.** 9, 2006, Appl. Phys. Lett., Vol. 89.

6. *Nanoscale imaging of domain dynamics and retention in ferroelectric thin films.* **A. Gruverman, H. Tokumoto, A. Prakash, S. Aggarwal, B. Yang, M. Wuttig, R. Ramesh, O. Auciello, T. Venkatesan.** 24, 1997, Appl. Phys. Lett., Vol. 71, pp. 3492-3494.

7. *Revealing the role of defects in ferroelectric switching with atomic resolution.* **P. Gao, C. Nelson, J. Jokisaari, S. Baek, C. Bark, Y. Zhang, E. Wang, D. Schlom, C. Eom, X. Pan.** 1, 2011, Nat. Commun., Vol. 2, p. 591.

8. *Nanoscale insight into the statics and dynamics of polarization behavior in thin film ferroelectric capacitors.* **Gruverman, A.** 2009, J. Mater. Sci., Vol. 44, pp. 5182-5188.

9. *Direct imaging of the spatial and energy distribution of nucleation centres in ferroelectric materials.* **S. Jesse, B. Rodriguez, S. Choudhury, A. Baddorf, I. Vrejoiu, D. Hesse, M. Alexe, E. Eliseev, A. Morozovska, J. Zhang, L.-Q. Chen, S. Kalinin.** 3, 2008, Nat. Mater., Vol. 7, pp. 209-215.

10. *Defect-Mediated Polarization Switching in Ferroelectrics and Related Materials: From Mesoscopic Mechanisms to Atomistic Control.* **S. Kalinin, B. Rodriguez, A. Borisevich, A. Baddorf, N. Balke, H. Chang, L.-Q. Chen, S. Choudhury, S. Jesse, P. Maksymovych, M. Nikiforov, S. Pennycook.** 3, 2010, Adv. Mater., Vol. 22, pp. 314-322.

11. *Contribution of the irreversible displacement of domain walls to the piezoelectric effect in barium titanate and lead zirconate titanate ceramics.* **D. Damjanovic, M. Demartin.** 23, 1997, J. Phys.: Condens. Matter, Vol. 9, p. 4943.

12. *Intrinsic and extrinsic eize effects in fine-grained morphotropic-phase-boundary lead zirconate titanate ceramics.* **C. Randall, N. Kim, J. Kucera, W. Cao, T. Shrout.** 3, 1998, J. Am. Ceram. Soc., Vol. 81, pp. 677-688.

13. *Grain size dependence of properties in lead nickel niobate-lead zirconate titanate films.* **F. Griggio, S. Trolier-McKinstry.** 2, 2010, J. Appl. Phys., Vol. 107.

14. *First-principles study of the interplay between grain boundaries and domain walls in ferroelectric PbTiO3.* **P. Marton, T. Shimada , T. Kitamura , C. Elsässer.** 6, 2011, Phys. Rev. B, Vol. 83, p. 064110.

15. *Polarization switching kinetics of epitaxial Pb (Zr0.4 Ti0.6)O3 thin films.* **Y. So, D. Kim, T. Noh, J. Yoon, T. Song.** 9, 2005, Appl. Phys. Lett., Vol. 86.

16. *High speed SPM applied for direct nanoscale mapping of the Influence of defects on ferroelectric switching dynamics.* **B. Huey, R. Premnath, S. Lee, N. Polomoff.** 4, 2012, J. Am. Ceram. Soc., Vol. 95, pp. 1147-1162.

17. *A computational model of ferroelectric domains. Part I: model formulation and domain switching.* **W. Zhang, K. Bhattacharya.** 1, 2005, Acta Mater., Vol. 53, pp. 185-198.

18. *Phase-field simulation of polarization switching and domain evolution in ferroelectric polycrystals.* **S. Choudhury, Y. Li, C. Krill Iii, L. Chen.** 20, 2005, Acta Mater., Vol. 53, pp. 5313-5321.

19. *Effect of grain orientation and grain size on ferroelectric domain switching and evolution: Phase field simulations.* **S. Choudhury, Y. Li, C. Krill Iii, L. Chen.** 4, 2007, Acta Mater., Vol. 55, pp. 1415-1426.

20. *Grain size and domain size relations in bulk ceramic ferroelectric materials.* **W. Cao, C. Randall.** 10, 1996, J. Phys. Chem. Solids, Vol. 57, pp. 1499-1505.

21. *The continuity of ferroelectric domains at grain boundaries in lead zirconate titanate.* **S. Tsurekawa, K. Ibaraki, K. Kawahara, T. Watanabe.** 7, 2007, Scr. Mater., Vol. 56, pp. 577-580.

22. *Ferroelectric domain continuity over grain boundaries.* **S. Mantri, J. Oddershede, D. Damjanovic, J. Daniels.** 2017, Acta Mater., Vol. 128, pp. 400-405.

23. *Collective dynamics underpins Rayleigh behavior in disordered polycrystalline ferroelectrics.* **P. Bintachitt, S. Jesse, D. Damjanovic, Y. Han, I. Reaney, S. Trolier-McKinstry, S. Kalinin.** 16, 2010, PNAS, Vol. 107, pp. 7219-7224.

24. *Rayleigh law response in ferroelectric ceramics: quantifying domain wall dynamics and structural relationships.* **Eitel, R.** 2007, IEEE ISAF, pp. 319-323.

25. *Influence of doping and thickness on domain avalanches in lead zirconate titanate thin films.* **T. Peters, W. Zhu, M. Checa, L. Collins, S. Trolier-McKinstry.** 13, 2023, Appl. Phys. Lett., Vol. 122.

26. *Substrate clamping effects on irreversible domain wall dynamics in lead zirconate titanate thin films.* **F. Griggio, S. Jesse, A. Kumar, O. Ovchinnikov, H. Kim, T. Jackson, D. Damjanovic, S. Kalinin, S. Trolier-McKinstry.** 15, 2012, Phys. Rev. Lett., Vol. 108, p. 157604.

27. *Designing piezoelectric films for micro electromechanical systems.* **S. Trolier-McKinstry, F. Griggio, C. Yaeger, P. Jousse, D. Zhao, S. Bharadwaja, T. Jackson, S. Jesse, S. Kalinin, K. Wasa.** 9, 2011, IEEE T-UFFC, Vol. 58, pp. 1782-1792.

28. *Direct observation of asymmetric domain wall motion in a ferroelectric capacitor.* **J. Lee, G. Shin, K. Song, W. Choi, Y. Shin, S. Park, J. Britson, Y. Cao, L.-Q. Chen, H. Lee, S. Oh.** 18, 2013, Acta Mater., Vol. 61, pp. 6765-6777.

29. *Domain patterns in epitaxial rhombohedral ferroelectric films. I. Geometry and experiments.* **S. Streiffer, C. Parker, A. Romanov, M. Lefevre, L. Zhao, J. Speck, W. Pompe, C. Foster, G. Bai.** 5, 1998, J. Appl. Phys., Vol. 83, pp. 2742-2753.

30. *Real-time studies of ferroelectric domain switching: a review.* **L. Li, L. Xie, X. Pan.** 12, 2019, Rep. Prog. Phys., Vol. 82, p. 126502.

31. *Domain wall motion across microstructural features in polycrystalline ferroelectric films.* **G. Hennessey, T. Peters, P. Tipsawat, M. Checa, L. Collins, S. Trolier-McKinstry.** 2023, Acta. Mater., Vol. 250, p. 118871.

32. *Influence of a Single Grain Boundary on Domain Wall Motion in Ferroelectrics.* **D. Marincel, H. Zhang, A. Kumar, S. Jesse, S. Kalinin, W, Rainforth, I. Reaney, C. Randall, S. Trolier-McKinstry.** 10, 2014, Adv. Func. Mater., Vol. 24, pp. 1409-1417.

33. *Domain pinning near a single-grain boundary in tetragonal and rhombohedral lead zirconate.* **D. Marincel, H. Zhang, J. Briston, A. Belianinov, S. Jesse, S. Kalinin, L. Chen, W. Rainforth, I. Reaney, C. Randall, S. Trolier-McKinstry.** 13, 2015, Phys. Rev. B, Vol. 91, p. 134113.

34. *Domain Wall Motion Across Various Grain Boundaries in Ferroelectric Thin Films.* **D. Marincel, H. Zhang, S. Jesse, A. Belianinov, M. Okatan, S. Kalinin, W. Rainforth, I. Reaney, C. Randall, S. Trolier-McKinstry.** 6, 2015, J. Am. Ceram. Soc., Vol. 98, pp. 1848-1857.

35. *Probing nanoscale structure and strain by dark-field x-ray microscopy.* **C. Yildirim, P. Cook, C. Detlefs, H. Simons, H. Poulsen.** 4, 2020, MRS Bulletin, Vol. 45, pp. 277-282.

36. *Long-range symmetry breaking in embedded ferroelectrics.* **H. Simons, A. Haugen, A. Jakobsen, S. Schmidt, F. Stöhr, M. Majkut, C. Detlefs, J. Daniels, D. Damjanovic, H. Poulsen.** 9, 2018, Nat. Mater., Vol. 17, pp. 814-819.

37. *The technique of studying X-ray scattering over wide temperature range in an electric field.* **S. Udovenko D. Chernyshov, D. Andronikova, A. Filimonov, S. Vakhrushev.** 2018, Solid State Phys., Vol. 60, pp. 963-966.

38. *Electric field control of antiferroelectric domain pattern.* **S. Vakhrushev, D. Andronikova, Yu. Bronwald, E. Koroleva, D. Chernyshov, A. Filimonov, S. Udovenko, A. Rudskoy, D. Ishikawa, A. Baron, A. Bosak, I. Leontiev A. Tagantsev.** 21, 2021, Phys. Rev. B, Vol. 103, p. 214108.

39. *Combining Nanofocused X-Rays with Electrical Measurements at the NanoMAX Beamline.* **L. Chayanun, S. Hammarberg, H. Dierks, G. Otnes, A. Björling, M. Borgström, J. Wallentin.** 8, 2019, Cryst., Vol. 9, p. 432.

40. *X-ray nanodiffraction of tilted domains in a poled epitaxial BiFeO3 thin film.* **S. Hruszkewycz, C. Folkman, M. Highland, M. Holt, S. Baek, S. Streiffer, P. Badlo, C. Eom, P. Fuoss.** 23, 2011, Appl. Phys. Lett., Vol. 99.

41. *Universal phase dynamics in VO2 switches revealed by ultrafast operando diffraction.* **A. Sood, X. Shen, Y. Shi, S. Kumar, S. Park, M. Zajac, Y. Sun, L.-Q. Chen, S. Ramanathan, X. Wang, W. Chueh, A. Lindenberg.** 6552, 2021, Science, Vol. 373, pp. 352-355.

42. *Infrared Nanoimaging of Hydrogenated Perovskite Nickelate Memristive Devices.* **S Gamage, S. Manna, M. Zajac, S. Hancock, Q. Wang, S. Singh, M. Ghafariasl, K. Yao, T. Tiwald, T. Park, D. Landau, H. Wen, S. Sankaranarayanan, P. Darancet, S. Ramanathan, Y. Abate.** 3, 2024, ACS nano, Vol. 18, pp. 2105-2116.

43. *The effect of imprint on remanent piezoelectric properties and ferroelectric aging of PbZr0.52Ti0.48O3 thin films.* **B. Akkopru-Akgun, W, Zhu, M. Lanagan, S. Trolier-McKinstry.** 9, 2019, J. Am. Ceram. Soc., Vol. 102, pp. 5328-5341.

44. *Domain wall contributions to the properties of piezoelectric thin films.* **N. Bassiri-Gharb, I. Fujii, E. Hong, S. Trolier-McKinstry, D. Taylor, D. Damjanovic.** 2007, J. Electroceram., Vol. 19, pp. 49-67.

45. *Chemically prepared Pb (Zr, Ti) O/sub 3/thin films: the effects of orientation and stress.* **B. Tuttle, J. Voigt, T. Garino, D. Goodnow, R. Schwartz, D. Lamppa, T. Headley, M. Eatough.** 1992, ISAF '92, pp. 344-348.

46. *Epitaxial PZT films for MEMS printing applications.* **H. Funakubo, M. Dekkers, A. Sambri, S. Gariglio, I. Shklyarevskiy, G. Rijnders.** 11, 2012, MRS bulletin, Vol. 37, pp. 1030-1038.

47. *Effect of stresses on the dielectric and piezoelectric properties of Pb(Zr0.52Ti0.48)O3 thin films.* **K. Coleman, J. Walker, T. Beechem, S. Trolier-McKinstry.** 3, 2019, J. Appl. Phys, Vol. 126.

48. *Residual Stress and Ferroelastic Domain Reorientation in Declamped {001} Pb(Zr0.3Ti0.7)O3 Films.* **L. Denis-Rotella, G. Esteves, J. Walker, H. Zhou, J. Jones, S. Trolier-McKinstry.** 2, 2020, IEEE T-UFFC, Vol. 68, pp. 259-272.

49. *The expected uncertainty of diffraction-peak location.* **M. Daymond, P. Withers, M. Johnson.** 2002, Appl. Phys. A, Vol. 74, pp. 112-114.

50. *Longitudinal piezoelectric coefficient measurement for bulk ceramics and thin films using pneumatic pressure rig.* **F. Xu, F. Chu, S. Trolier-McKinstry.** 1, 1999, J. Appl. Phys., Vol. 86, pp. 588-594.

51. *Origins of electro-mechanical coupling in polycrystalline ferroelectrics during subcoercive electrical loading.* **A. Pramanick, D. Damjanovic, J. Daniels, J. Nino, J. Jones.** 2, 2011, J. Am. Ceram. Soc., Vol. 94, pp. 293-309.

52. *Domain texture distributions in tetragonal lead zirconate titanate by x-ray and neutron diffraction.* **J. Jones, E. Slamovich, K. Bowman.** 3, 2005, J. Appl. Phys., Vol. 97.

53. *Quantifying Domain Textures in Lead Zirconate Titanate Using 022:202 and 220 Diffraction Peaks.* **T. Key, J. Jones, W. Shelley, K. Bowman.** 2005, Solid State Phenom., Vol. 105, pp. 379-384.

54. *Structural investigations on Pb(ZrxT1−x)O3 solid solutions using the X-ray Rietveld method.* **J. Joseph, T. Vimala, V. Sivasubramanian, V. Murphy.** 2000, J. Mater. Sci., Vol. 35, pp. 1571-1575.